The Journal of Experimental Biology 211, 3181-3194
Published by The Company of Biologists 2008
doi:10.1242/jeb.019844

The kinematic determinants of anuran swimming performance: an inverse and forward dynamics approach

Christopher T. Richards

Concord Field Station, Department of Organismic and Evolutionary Biology, Harvard University, Bedford, MA 01730, USA
e-mail: richards@fas.harvard.edu

Accepted 12 August 2008

SUMMARY

The aims of this study were to explore the hydrodynamic mechanism of *Xenopus laevis* swimming and to describe how hind limb kinematics shift to control swimming performance. Kinematics of the joints, feet and body were obtained from high speed video of *X. laevis* frogs (*N*=4) during swimming over a range of speeds. A blade element approach was used to estimate thrust produced by both translational and rotational components of foot velocity. Peak thrust from the feet ranged from 0.09 to 0.69 N across speeds ranging from 0.28 to 1.2 m s^{-1}. Among 23 swimming strokes, net thrust impulse from rotational foot motion was significantly higher than net translational thrust impulse, ranging from 6.1 to 29.3 N ms, compared with a range of –7.0 to 4.1 N ms from foot translation. Additionally, *X. laevis* kinematics were used as a basis for a forward dynamic anuran swimming model. Input joint kinematics were modulated to independently vary the magnitudes of foot translational and rotational velocity. Simulations predicted that maximum swimming velocity (among all of the kinematics patterns tested) requires that maximal translational and maximal rotational foot velocity act in phase. However, consistent with experimental kinematics, translational and rotational motion contributed unequally to total thrust. The simulation powered purely by foot translation reached a lower peak stroke velocity than the pure rotational case (0.38 *vs* 0.54 m s^{-1}). In all simulations, thrust from the foot was positive for the first half of the power stroke, but negative for the second half. Pure translational foot motion caused greater negative thrust (70% of peak positive thrust) compared with pure rotational simulation (35% peak positive thrust) suggesting that translational motion is propulsive only in the early stages of joint extension. Later in the power stroke, thrust produced by foot rotation overcomes negative thrust (due to translation). Hydrodynamic analysis from *X. laevis* as well as forward dynamics give insight into the differential roles of translational and rotational foot motion in the aquatic propulsion of anurans, providing a mechanistic link between joint kinematics and swimming performance.

Key words: blade element model, forward dynamic model, hydrodynamics, frog, *Xenopus laevis*

INTRODUCTION

Aquatic invertebrates and vertebrates commonly use oscillating paired limbs for propulsion. For example, rowing animals such as larval insects, fish and mammals rotate their limbs in a cranio-caudal direction to create thrust (e.g. Blake, 1985; Blake, 1979; Fish et al., 1997). These animals, often called 'drag-based' swimmers, rely on resistive hydrodynamic forces to swim (Daniel, 1984; Vogel, 1994). Alternatively, other paired-limb swimmers generate 'lift-based' propulsion by the use of modified morphology and kinematics allowing propulsive limbs to move dorso-ventrally (e.g. Walker and Westneat, 2002; Johansson and Norberg, 2003). This has stimulated studies investigating how lift- *vs* drag-based swimming relates to propulsive efficiency and swimming speed (Vogel, 1994; Fish, 1996; Walker and Westneat, 2000). More recent work has proposed that frog feet generate lift; however, no evidence for 'lift-based' propulsion has been found in swimming anurans (Johansson and Lauder, 2004; Nauwelaerts et al., 2005). More broadly, these studies relate the kinematics of limb motion to hydrodynamics as well as swimming performance. Using swimming frogs as a model, the current study expands on previous work by exploring how swimmers control different components of motion (i.e. foot rotation and translation) in order to modulate hydrodynamic forces and swimming performance.

In addition to simple cranio-caudal rotation in rowing, aquatic tetrapod limbs use joints to further control the propulsor's position with respect to the body. For example, swimming turtles use proximal joints to control the medio-lateral position of the forefeet to maximize drag-based thrust during caudal limb rotation, but minimize drag during the recovery stroke (Pace et al., 2001). Diving grebes (*Podiceps cristatus*) also benefit from the additional range of motion, generating lift-based thrust by using proximal joints (causing backward and upward foot motion) while rotating the feet at distal joints (Johansson and Lindhe Norberg, 2001). Given that jointed limbs confer diverse swimming modes among species, is kinematic variability a means for controlling swimming performance within a species? In addition, do the relative roles of limb joints shift across different swimming behaviors to enable a broad range of performance within individuals?

Studies of terrestrial locomotion have addressed how the functions of different limb joints change to enable increases in speed (e.g. Dutto et al., 2006), incline (e.g. Roberts and Belliveau, 2005), acceleration (Roberts and Scales, 2004; McGowan et al., 2005) and stabilizing responses to substrate height perturbations (Daley et al., 2007). Such studies have shown that partitioning of limb function (e.g. mechanical work production, absorption, stabilization) occurs across individual limb joints. For example, in wallabies, the ankle serves to store and return elastic energy during steady speed locomotion (Biewener and Baudinette, 1995). However, during acceleration the roles of hind limb joints in turkeys and wallabies change, with the ankle providing most of the increased mechanical

work required to increase speed (Roberts and Scales, 2004; McGowan et al., 2005). Similarly, the ankle shifts from elastic energy recovery (producing little net joint work) during steady level running in guinea fowl, to energy absorption following an unexpected drop in substrate height (Daley et al., 2007). By analogy, limb joints during swimming may also have distinct functions (e.g. work production, energy transmission between joints, or joint stabilization). Presumably, these roles can change according to varying mechanical demands across different swimming tasks (e.g. predator escape, prey capture and steady swimming). Understanding how musculoskeletal dynamics enable diverse swimming behaviors is therefore important for understanding the evolutionary and ecological diversity of aquatic vertebrates.

Aquatic frogs are ideal models for exploring the differential use of limb joints to modulate swimming performance. For example, work by Nauwelaerts and Aerts addressed functions of anuran hind limb joints in swimming *vs* jumping to explore how hind limb mechanics enable function across ecological performance space (Nauwelaerts and Aerts, 2003). They used a novel and elegant approach of analyzing joint kinematics patterns as functions of both propulsive impulse ('locomotor effort') and locomotor mode. Their findings demonstrate that kinematic variation within a locomotor mode (explained by variation in propulsive impulse) can confound comparisons between jumping and swimming kinematics. Consequently, their work gives compelling evidence that anurans modulate limb kinematics to enable a range of performance within as well as between locomotor modes. However, the mechanistic link between time-varying patterns of joint motion and performance has not yet been explicitly examined in swimming frogs.

Given the potential range of kinematics patterns available to frog hind limbs (Kargo and Rome, 2002), resolving the functional roles of individual joints may be a daunting task. However, frog hind limbs move mostly in the frontal plane during swimming (i.e. within the plane defined by the cranio-caudal and medio-lateral axes) (Peters et al., 1996). Therefore, the joint motions can be summed into three components: cranio-caudal foot translation, medio-lateral foot translation (each caused by hip and knee rotation) and cranio-caudal foot rotation (from ankle and tarsometatarsal joint rotation). Several recent studies have speculated on the importance of translational foot motion, observing that the foot is swept through the water at nearly 90 deg. to flow for most of the power stroke, with rotation delayed towards the end of limb extension (Peters et al., 1996; Nauwelaerts et al., 2005). This suggests that foot rotation (*via* ankle extension) need not directly aid in propulsion. Instead, the role of foot rotation may be to straighten the foot parallel to flow to minimize drag just prior to the glide phase (Peters et al., 1996; Johansson and Lauder, 2004; Nauwelaerts et al., 2005). Johansson and Lauder further suggest that foot rotation serves to shed the attached vortex from the foot, minimizing a retarding hydrodynamic force incurred from fluid added mass as the foot decelerates late in the propulsive phase (Johansson and Lauder, 2004).

Building on this earlier work, my study tests the hypothesis that propulsion in *Xenopus laevis* is powered primarily by hip and knee extension (causing foot translation) rather than foot rotation produced at the ankle. Increases in speed from stroke to stroke, therefore, are expected to be powered mainly by increases in translational thrust from the foot. For the present study, a blade element model modified from an earlier study (Gal and Blake, 1988b) was used to dissect the components of thrust due to foot translation and rotation. Additionally, the blade element kinematic analysis was coupled with a forward dynamic approach to create a generalized anuran swimming model. This simulation allowed the modulation of swimming performance through manipulation of hind limb kinematic patterns. Along with a prior study of plantaris longus muscle function during *X. laevis* swimming (Richards and Biewener, 2007), the current study provides a framework for interpreting the role of muscle function in the context of the complex kinematics of jointed appendages.

MATERIALS AND METHODS

Anuran swimming model

Spatial dimensions of the anuran swimming model were based on morphological measurements obtained from adult male *Xenopus laevis* (Daudin 1802) frogs (25.5±3.8 g mean ± s.d. body mass; 6.1±0.5 cm snout–vent length; N=4 frogs). Frog morphology was modeled as an ellipsoid body attached to two legs, each with pin joints at the hip, knee and ankle connected by two cylindrical segments (Fig. 1). Foot area was calculated digitally by tracing an image of individual *Xenopus laevis* feet (spread flat on a white surface) using Scion Image (Scion Corporation, Frederick, MD, USA). A trapezoidal flat plate of the same foot area was used in the model to approximate the foot's shape.

Model calculations consisted of two parts: (1) an inverse approach, which estimated the hydrodynamic thrust forces at the feet based on prescribed joint kinematics (based on *X. laevis* kinematics) and (2) a forward approach, which simulated the swimming velocity profile of the frog due to the hydrodynamic and inertial forces acting on the body.

Inverse model: estimating propulsive forces from joint kinematics input

Thrust was estimated as the sum of two independent hydrodynamic forces acting at the feet: drag and added mass (Daniel, 1984; Gal and Blake, 1988b). In this model, the feet were the only propulsive surfaces (i.e. propulsive hydrodynamic effects of the cylindrical leg segments were not considered). Propulsion was driven by extension of the hip and knee, causing both lateral and aft-directed foot translation, as well as at the ankle, causing foot rotation. All equations, therefore, could be expressed in terms of translational velocity aft to the center of mass ($\mathbf{v}_t$), lateral translational velocity ($\mathbf{v}_l$), rotational velocity about the ankle joint ($\mathbf{v}_r$) and velocity of the center of mass ($\mathbf{v}_{COM}$) (Fig. 1). In the current study, all velocity components of the hind limb were defined with respect to the coordinate system illustrated in Fig. 1. Therefore, aft-directed foot translational velocity was positive. The drag-based thrust force on each foot was estimated from a blade element model modified from (Gal and Blake, 1988b):

$$\mathbf{T}_{Drag} = \rho C_D \sin\theta_f \int_0^c \left(\frac{b-a}{c} r + a\right)[r\mathbf{v}_r + (\mathbf{v}_t - \mathbf{v}_{COM})]^2 \, dr \ , \quad (1)$$

where ρ is the water density, θ_f is the foot angle measured from the body midline, r is the distance along the foot, $\mathbf{v}_r$ and $\mathbf{v}_t$ are the velocity components defined above and a, b and c are dimensions of the foot (assumed to be symmetric about its mid-axis; see Fig. 1). Due to a lack of published literature addressing the coefficient of drag (C_D) of a translating and rotating plate in the range of Reynolds number (Re) of *Xenopus laevis* feet (Re ~1000 to 20,000), C_D was set constant at 2.0, the maximum value for a flat plate at 90 deg. angle of attack at Re=10^3 (Andersen et al., 2005). A sensitivity analysis to C_D was performed by running 500 model iterations while randomly varying the C_D between 1.1 (Gal and Blake, 1988b) and 2.0 at each iteration. All other input parameters (e.g. foot kinematics, added mass coefficients) were left unchanged. Simulated variation in C_D resulted in a negligible (<2%) variation in the net drag produced during the

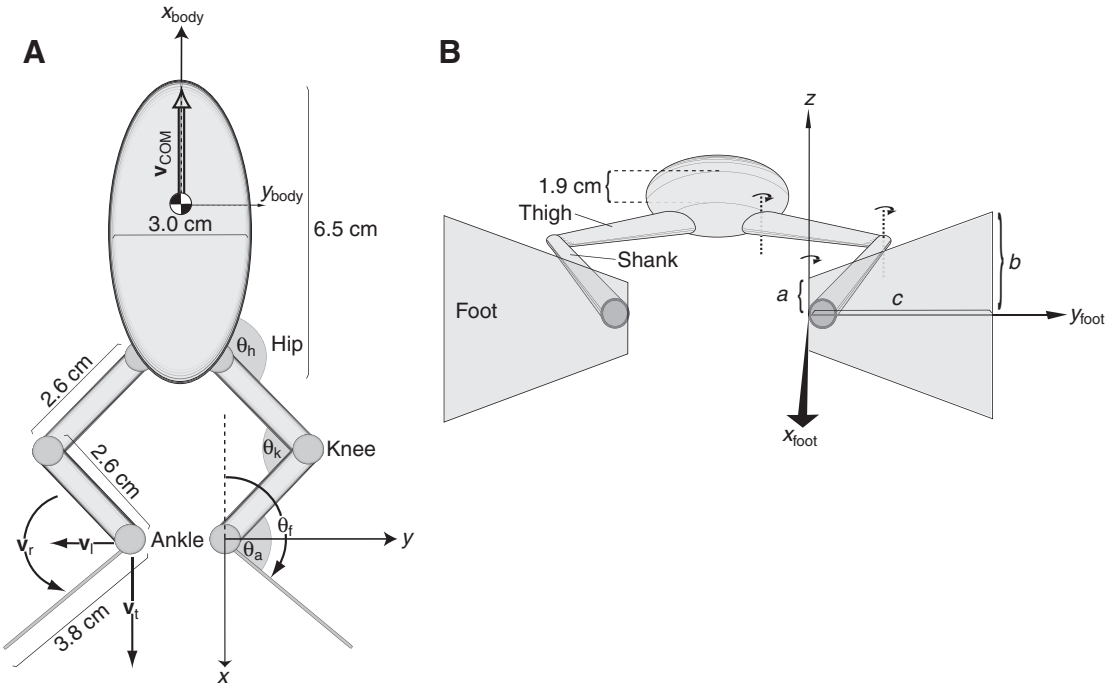

Fig. 1. Anuran model morphology. (A) Dorsal view showing an ellipsoid body and cylindrical leg segments connected to two thin plate feet. Foot velocity components are also shown: cranio-caudal translational velocity ($\mathbf{v}_t$), medio-lateral translational velocity ($\mathbf{v}_l$) and rotational velocity ($\mathbf{v}_r$). The foot angle (θ_f) is defined with respect to the body midline, and $\mathbf{v}_{COM}$ denotes the forward swimming velocity of the body (COM, center of mass). Joint angles at the hip (θ_h), knee (θ_k) and ankle (θ_a) are indicated with shaded discs. (B) Posterior view showing the shape and dimensions of the feet. The coordinate system used for added mass calculations is shown by arrows for aft-directed translation (*x*), lateral translation (*y*) and a rotational axis (*z*) about the ankle. A separate coordinate system is used for the motion of the body. Velocity in the direction of the arrows is defined as positive in their respective coordinate systems. All dimensions shown correspond to measurements taken from frog 1. Note that all limb movements are constrained to occur in the frontal (*x*–*y*) plane. *a*–*c*, dimensions of the foot.

stroke, suggesting that the findings predicted by the model are insensitive to variation in C_D within the range of 1.1 to 2.0.

From the added mass coefficients (m), added mass thrust was calculated (see Appendix A) as:

$$\mathbf{T}_{amass} = 2(\dot{v}_n m_{11} + \mathbf{v}_l \mathbf{v}_r m_{22} + \dot{v}_r m_{61}) , \quad (2)$$

where $\mathbf{v}_n$ is net translational velocity ($\mathbf{v}_t$–$\mathbf{v}_{COM}$), with total thrust produced at the feet calculated as:

$$\mathbf{T} = \mathbf{T}_{Drag} + \mathbf{T}_{amass} . \quad (3)$$

Forward model: simulating swimming velocity from joint kinematics input

A forward dynamics approach was used to computationally solve the time-varying acceleration and velocity of the frog body due to the time-varying thrust estimated at the foot (Eqns 1 and 2). The following equations were used (Nauwelaerts et al., 2001):

$$\dot{v}_{frog} = \frac{1}{m_{frog}(1 + C_{amass})} (\mathbf{T} + \mathbf{D}) , \quad (4)$$

given:

$$\mathbf{D} = \frac{1}{2} \rho A C_{D,body} \mathbf{v}_{frog}^2 , \quad (5)$$

where A is the area of the frog body projected onto the animal's transverse plane, $C_{D,body}$ is the body coefficient of drag, C_{amass} is the added mass coefficient of the body, m_{frog} is the frog mass, **T** is the propulsive force produced by both feet (Eqn 3 above), **D** is the drag on the frog body and $\mathbf{v}_{frog}$ is the frog's simulated swimming velocity. Coefficient values C_{amass}=0.2 and $C_{D,frog}$=0.14 were taken from previous studies (Nauwelaerts et al., 2001; Nauwelaerts and Aerts, 2003). Since swimming acceleration and thrust are functions of one another, the coupled ordinary differential equations (Eqns 1, 4 and 5) were solved simultaneously using a numerical equation solver in Mathematica 6.0 (Wolfram Research, Champaign, IL, USA).

Model verification: predicting swimming velocity from foot kinematics

To verify the numerical model, *Xenopus laevis* swimming was recorded for four individuals across the entire range of their performance (from slow swimming to rapid escape swimming). Joint kinematics data were measured from video sequences filmed from a dorsal view at 125 frames s^{-1} with a 1/250 s shutter speed using a high speed camera (Photron, San Diego, CA, USA), as detailed in a previous study (Richards and Biewener, 2007). Small plastic markers (0.5 cm diameter) were placed on the snout, vent, knee, ankle and tarsometatarsal joint using a cyanoacrylate adhesive. Foot kinematics were digitized in Matlab (The MathWorks, Natick, MA, USA) using a customized routine (DLTdataviewer 2.0 written by Tyson Hedrick). Only strokes with a straight swimming trajectory were analyzed.

Due to the large mass of the legs (~11% of body mass), the position of the center of mass (COM) was assumed to vary depending on the position of the legs behind the body. Using a dead frog, the position of the COM (relative to the snout) was measured with the ankle joint moved to various distances caudal to the vent

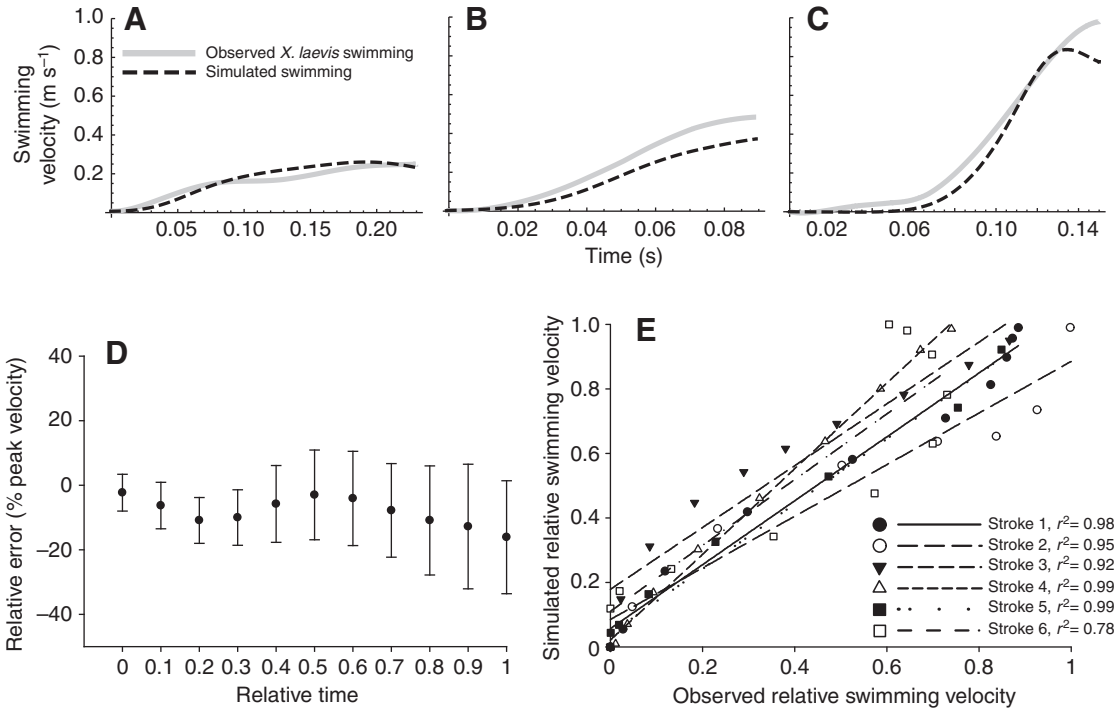

Fig. 2. Verification of the numerical model. Observed *Xenopus laevis* swimming velocity (solid gray lines) and simulated velocity traces (dashed black lines) of three representative power strokes during (A) slow swimming, (B) moderate speed swimming and (C) fast swimming. Note that each stroke occurred over a different duration. (D) Relative model error [100%×(simulated velocity−observed velocity)/peak observed stroke velocity] at 10 time points of the power stroke (mean ± s.d., *N*=6 strokes; frog 1). Because stroke durations were variable, the 10 time points were normalized by the total duration of each power stroke. Note that all data points are, on average, slightly below zero relative error, indicating that the model generally underestimates swimming velocity at each time point during the stroke. (E) Simulated relative swimming velocity (simulated swimming velocity/observed peak stroke velocity) *vs* observed relative swimming velocity (observed swimming velocity/observed peak stroke velocity) for the six swimming strokes represented in D, from frog 1. Different symbols represent different strokes.

of the body (see Walter and Carrier, 2002). Using the measured relationship between the position of the ankle (relative to the vent) and the COM on the dead frog, the instantaneous COM position on swimming frogs was estimated from the known aft translational displacement of the foot.

To minimize error in setting the initial conditions of the forward dynamic simulation, a subset of six swimming strokes were selected where the animal began swimming from a rest position (initial COM velocity=0). Joint kinematics traces were smoothed using a second order forward–backward 20 Hz low-pass Butterworth filter before calculating translational and rotational velocities and accelerations of the foot. All data processing was done in Labview 7.1 (National Instruments, Austin, TX, USA). Hind limb kinematics (θ_f, $\mathbf{v}_t$, $\mathbf{v}_r$, $\mathbf{v}_l$, $\dot{v}_t$, $\dot{v}_r$, $\dot{v}_l$) for six trials were then input into the swimming model (see above) to predict the frog's swimming velocity and acceleration output (Fig. 2A–C). Only the power stroke, defined as the period of positive COM acceleration (i.e. the period between the onset of swimming and peak COM velocity), was analyzed. Simulated and observed COM velocity profiles were then compared to verify the model.

Estimating net joint work and hydrodynamic efficiency

As an index of overall muscular effort required to extend the hip, knee and ankle to power swimming, estimates of net joint work were obtained by inverse dynamics (not to be confused with the inverse approach used to estimate hydrodynamic forces from foot kinematics; see above). The net work required at a given joint is the sum of internal work (from the inertia of the segments), external work (from the thrust reaction force at the foot), and hydrodynamic work (from the hydrodynamic forces acting directly on the segments; see Appendix B). The thigh and shank were modeled as cylinders (Fig. 1A) with uniformly distributed mass, such that the COM lies at the center of each segment length. Segment masses were measured from the *Xenopus laevis* frog used above. Internal and external moments were calculated according to Biewener and Full (Biewener and Full, 1992). The internal moment due to inertia of the thigh and shank was calculated as follows:

$$\mathbf{M}_{\text{internal}} = \sum_{i=1}^{n} I_i + m_i r_i^2 \alpha_i \ , \qquad (6)$$

where I is the segment's moment of inertia, m is the segment's mass, r is the distance from the joint's center of rotation to the segment COM and α is the segment's angular acceleration, summed over i=1 to n joint segments distal to the joint of interest (see Appendix B for further details). The external moment required at each joint to resist hydrodynamic forces at the foot was calculated and the total moment at each joint was then obtained:

$$\mathbf{M}_{\text{external}} = \mathbf{F}_{\text{foot}} R \qquad (7)$$

and

$$\mathbf{M}_{\text{total}} = \mathbf{M}_{\text{internal}} + \mathbf{M}_{\text{external}} + \mathbf{M}_{\text{hydrodynamic}} \ , \qquad (8)$$

where $\mathbf{F}_{\text{foot}}$ is the total estimated force on the foot from the blade element model (see Gal and Blake, 1988b), R is the perpendicular distance between the $\mathbf{F}_{\text{foot}}$ vector (acting at the center of pressure on the foot) and the joint of interest, and $\mathbf{M}_{\text{hydrodynamic}}$ is the moment due

to hydrodynamic forces acting directly on the segments (see Appendix B). Instantaneous power required to overcome the total joint moment was modified from Roberts and Scales (Roberts and Scales, 2004):

$$\mathbf{P}_{\text{total}} = \mathbf{M}_{\text{total}}\,\omega\,, \tag{9}$$

where ω is the angular velocity of the joint of interest. To follow, the net work required to move a given joint is:

$$W_{\text{total}} = \int_0^{t_{\text{ps}}} \mathbf{P}_{\text{total}}\,\mathrm{d}t\,, \tag{10}$$

where t_{ps} is the duration of the power stroke. An estimate of hydrodynamic efficiency was obtained by dividing the work done to move the COM (the time-averaged force on the body during the power stroke × the total distance traveled) by the estimated net joint work summed for all joints.

Hypothetical performance space

The effects of varying the relative magnitude of translational and rotational foot velocity on swimming performance (e.g. peak stroke velocity) were explored by running simulated power strokes across the entire observed range of translational and rotational velocity in 33 increments, generating a 33×33 matrix of unique input conditions (i.e. 1089 simulated swimming strokes). Partial least squares regression was used to evaluate the relative contributions of translational or rotational velocity on swimming performance (Richards and Biewener, 2007).

Simulated foot kinematics

The range of input conditions in all swimming simulations was bounded by maximum translational and rotational velocities of $0.8\,\text{m}\,\text{s}^{-1}$ and $60\,\text{rad}\,\text{s}^{-1}$, respectively, obtained from *Xenopus laevis* foot velocity measurements of 35 swimming strokes spanning the entire range of performance of frog 1. Similar velocity ranges were found in the other three individuals used in this study. The power stroke of anuran swimmers is often followed by a period where the joints are held in fixed positions while the frog glides. Since the motion of the feet is impulsive (rather than periodic), simple sine/cosine functions are inadequate to describe the translational and rotational foot motion patterns. Hyperbolic tangent functions (as opposed to sine or cosine functions) were therefore used to approximate time-varying patterns of translational and rotational displacement of the foot:

$$\text{Translation}(t) = \frac{A_{\text{t}}}{2} - \frac{1}{2}A_{\text{t}}\tanh\left[\frac{\pi(t-0.5t_{\text{ps}})}{t_{\text{ps}}}\right] \tag{11}$$

and

$$\text{Rotation}(t) = \frac{A_{\text{r}}}{2} - \frac{1}{2}A_{\text{r}}\tanh\left[\phi - \frac{\pi(t-0.5t_{\text{ps}})}{t_{\text{ps}}}\right] + \theta_i\,, \tag{12}$$

where A_{t} and A_{r} are amplitudes of translational and angular displacements and t_{ps} is the duration of the power stroke. For each simulation, the initial foot angle, θ_{i}, was derived such that the foot angle was always at 90 deg. to the swimming direction at peak rotational and translational velocity. The phase angle between rotation and translation, ϕ, was set to 0 deg. for all of the simulations in this study. Translational and rotational velocities were modulated by varying the amplitudes of foot translation and angular displacement while maintaining a constant stroke period.

RESULTS

Verification of the numerical simulation

The numerical model reliably predicted the temporal pattern of the swimming velocity profiles of six swimming strokes (Fig. 2E); however, the magnitude of velocity was slightly underestimated in most strokes observed (Fig. 2D). At any given time point the average percentage error between the simulated profile and the observed data ranged from –2±6% at the beginning of the stroke to –16±18% at the end of the stroke (mean ± s.d., *N*=6 swimming strokes, frog 1; Fig. 2D). Most of the simulated velocity profiles averaged within ±15% of the observed data.

Xenopus laevis foot kinematics

In both representative slow and fast swimming strokes, foot velocity peaked prior to COM velocity (Fig. 3A,B). For the slow swimming stroke, translation and rotation were out of phase for the duration of the power stroke, with peak foot translational and rotational velocities occurring at 38% and 81% of the power stroke duration, respectively (Fig. 3A). During fast swimming, in contrast, translational and rotational foot velocity peaked in phase (Fig. 3B). For these representative strokes, peak translational and rotational foot velocities increased 1.7- and 2.1-fold, respectively, from the slow to fast swimming speeds.

Hydrodynamics of *Xenopus laevis* swimming: production of thrust by the feet

From slow to fast swimming, peak thrust increased from 0.09 to 0.49 N and net thrust impulse increased from 9.0 to 21.5 N ms. During both slow and fast swimming thrust developed rapidly at the onset of foot motion, accelerating the animal's COM early in the stroke (Fig. 4). Near the end of each stroke, as the hind limb approached peak extension, thrust decreased rapidly and became negative as the foot decelerated in translation and rotation. In all strokes observed, thrust peaked before COM velocity. However, the timing offset of peak thrust and peak swimming velocity varied among trials, as the time delay and relative magnitudes of translational and rotational foot velocity changed among trials (Fig. 3; Fig. 4A,B; Table 1).

Kinematic components of thrust: translational and rotational thrust

In all swimming strokes observed, propulsion was predominantly powered by rotational thrust. In all strokes observed, rotational impulse accounted for 93±24% of total thrust impulse (mean ± s.d., pooled data from 23 swimming strokes, *N*=4 frogs; Table 2). As exemplified by the two representative strokes chosen, the time-varying patterns of translational *vs* rotational thrust produced by the foot differed markedly in both slow and fast swimming. This variation accounted for differences in the relative contributions of rotational *vs* translational thrust to total thrust (Fig. 4A,B). Independent of swimming speed, translational thrust developed earliest, reaching a peak prior to rotational thrust. Subsequently, translational thrust of the foot rapidly diminished, becoming negative for the remainder of the stroke, resulting in a net negative translational impulse in the representative slow stroke. In contrast, rotational thrust of the foot was a significant component of total thrust, peaking later in the stroke and remaining positive for the duration of the power stroke. Because of the net negative translational impulse, total thrust impulse (translational + rotational impulse) was sometimes less than rotational impulse (Table 2). From slow to fast swimming, peak translational thrust increased 2.0-fold from 0.04 to 0.08 N and peak rotational thrust increased 4.4-fold from 0.11 to 0.48 N. In contrast, net translational impulse decreased

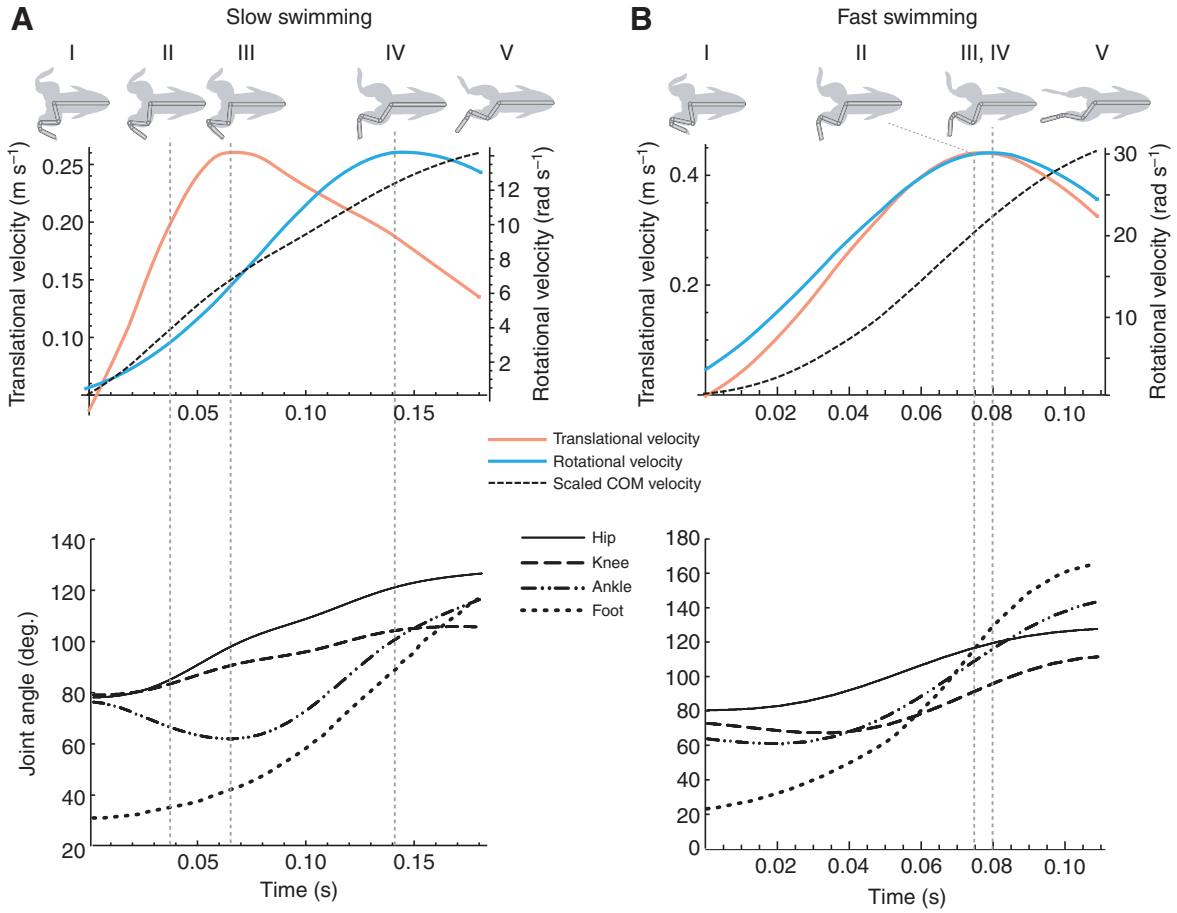

Fig. 3. Representative traces of *Xenopus laevis* kinematics for two power strokes. Each stroke was defined as the period of positive COM acceleration (i.e. the period between the onset of swimming and peak COM velocity). Foot translational velocity (solid red line) and rotational velocity (blue line) during (A) slow swimming and (B) fast swimming. Swimming velocity traces (dashed black line) were scaled to fit the data range shown. For A and B, outlines of *X. laevis* are shown at various stages during the power stroke: I, onset of swimming; II, peak COM acceleration; III, peak translational foot velocity; IV, peak rotational foot velocity; V, peak COM velocity (defined as the end of the power stroke). Joint angles for the hip (solid line), knee (dashed line), ankle (dash-dot line) and foot (dotted line) are shown in the lower panels of A and B.

3.0-fold from –1.9 to –6.3 N ms, whereas rotational impulse increased 2.5-fold from 11.0 to 27.0 N ms.

Hydrodynamic components of thrust: added mass and drag

Similar to the temporal pattern of translational thrust, added mass-based thrust only contributed to propulsion early in the stroke (Fig. 4C,D), rising to a peak in the first half of the propulsive period then decreasing to become negative at the end of limb extension, resulting in a net positive impulse of 1.1 *vs* 6.1 N ms in representative slow *vs* fast swimming strokes. Similarly, the pattern of drag-based thrust differed only slightly between slow and fast swimming strokes, peaking after mid-stroke, but becoming negative in the last 10% of each stroke (Fig. 4C,D). During slow swimming, added mass-based thrust peaked 28% of the stroke earlier than drag-based thrust. However, in fast swimming added mass-based thrust shifted later and drag-based thrust shifted earlier in the stroke, being nearly in phase for the representative fast stroke. Drag-based thrust dominated for both representative swimming speeds, producing an impulse of 7.8 N ms in slow and 15.1 N ms in fast swimming and accounting for 86% and 70% of total thrust impulse, respectively. Among all four animals observed, however, the relative contributions of drag-based and added mass-based thrust to total thrust impulse were highly variable. For three individuals (frogs 2, 3 and 4) net added mass-based impulse was not significantly different from net drag-based impulse (P>0.05; Table 3).

Kinematic components of added mass-based and drag-based thrust

Added mass-based thrust produced by translational motion gave a net negative impulse during the representative slow swimming stroke. Rotational added mass, however, was sufficient to overcome the negative translational added-mass impulse, causing the net added mass-based impulse to be positive. In contrast, translational and rotational motion contributed equally to the observed added mass-based impulse during fast swimming (Fig. 4E,F). Another notable difference was the phase offset of 31% *vs* 5% of translational and rotational added mass-based thrust in slow *vs* fast swimming, respectively.

Both representative slow and fast swimming strokes showed a high contribution of rotational motion to total drag-based thrust (Fig. 4G,H). In both slow and fast strokes, rotational drag was positive for the duration of the propulsive phase. From slow to fast swimming, net drag impulse due to rotation increased from 9.1 N ms to 24.2 N ms. However, translational drag was mostly negative, resulting in negative net impulses that decreased from –1.31 N ms to –9.18 N ms in slow *vs* fast swimming.

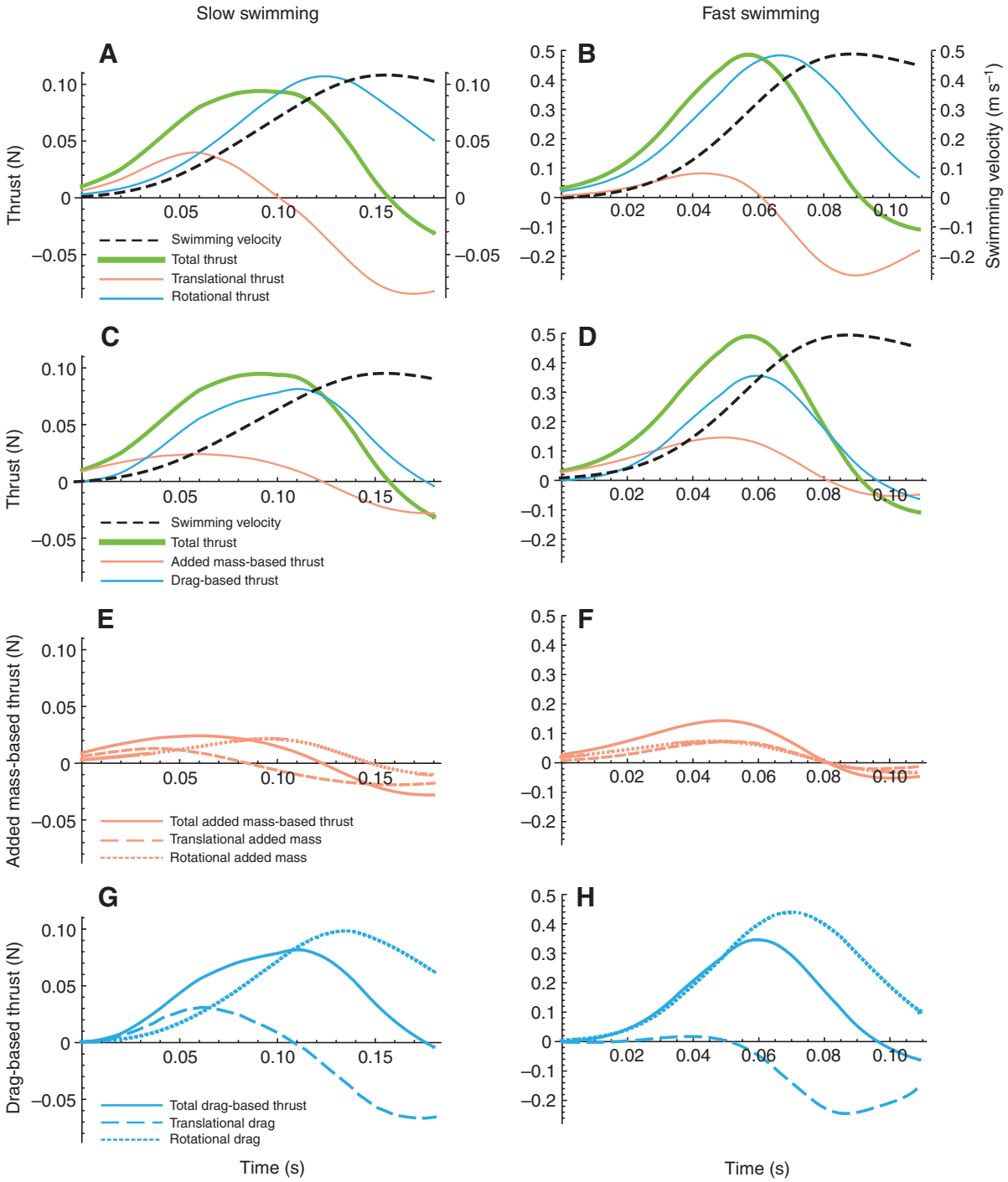

Fig. 4. Components of thrust in *Xenopus laevis* swimming. Total thrust (green line), translational thrust (red line) and rotational thrust (blue line) and swimming velocity (dashed black line) during (A) slow swimming and (B) fast swimming. (C) Total thrust (green line), added mass-based thrust (red line) and drag-based thrust (blue line) during slow swimming and (D) fast swimming. (E) Total added mass-based thrust (solid red line), and translational (dashed red line) and rotational added mass-based thrust (dotted red line) during slow swimming and (F) fast swimming. (G) Total drag-based thrust (solid blue line), and translational (dashed blue line) and rotational drag-based thrust (dotted blue line) during slow swimming and (H) fast swimming. Note that the green total thrust traces are identical in A and C as well as in B and D.

Simulated anuran swimming: modeling stroke-to-stroke modulation of swimming velocity

Modulating the relative magnitudes of translational and rotational velocity in the numerical model, as described above, caused marked differences in simulated swimming performance among power strokes (Fig. 5). The model predicted a maximal swimming velocity of 1.2 m s^{-1} with maximum translational and rotational velocities (0.8 m s^{-1} and 60 rad s^{-1}, respectively; Fig. 6). A simulation with pure rotational velocity (Fig. 5A) reached a peak swimming velocity of 0.54 m s^{-1} (45% of maximal velocity), whereas the simulation driven by pure translation only reached 31% of maximal velocity (Fig. 5C). In the intermediate case, with 50% maximum translational

Table 1. *Xenopus laevis* foot kinematics data summary

Frog	Number of strokes analyzed	Peak swimming velocity ($m\,s^{-1}$)	Peak translational velocity ($m\,s^{-1}$)	Peak rotational velocity ($rad\,s^{-1}$)	Rotation–translation phase offset (% stroke duration)*	Phase of peak thrust (% stroke duration)
1	6	0.55±0.26	0.35±0.11	23.84±9.28	15±21	48±12
2	6	0.49±0.19	0.41±0.17	28.21±6.18	25±8	50±14
3	6	0.63±0.20	0.44±0.15	25.99±7.34	13±10	42±12
4	5	0.56±0.34	0.43±0.21	25.00±4.08	25±12	61±2

All values are means ± s.d.
*Translation–rotation phase offset=100%×(time of peak rotational velocity – time of peak translational velocity)/stroke duration.

Table 2. Estimated thrust (**T**) and impulse (*I*) from *Xenopus laevis* feet during swimming

Frog	Peak **T** (N)	Peak $\mathbf{T}_{translational}$ (N)	Peak $\mathbf{T}_{rotational}$ (N)	I_{total} (N s)	$I_{translational}$ (N s)	$I_{rotational}$ (N s)	I_{amass} (N s)	I_{drag} (N s)
1	0.35±0.25	0.06±0.030	0.340±0.242	0.016±0.007	–0.004±0.003	0.019±0.009	0.004±0.003	0.0113±0.004
2	0.25±0.11	0.091±0.040	0.181±0.069	0.0137±0.004	0.002±0.001	0.011±0.003	0.004±0.002	0.009±0.005
3	0.36±0.18	0.133±0.051	0.255±0.151	0.016±0.007	0.002±0.003	0.014±0.006	0.009±0.004	0.007±0.004
4	0.19±0.13	0.0619±0.013	0.147±0.0595	0.010±0.003	0.0005±0.0008	0.008±0.001	0.004±0.001	0.004±0.002

Values are means ± s.d. amass is added mass.

Table 3. *P* values from Student's paired *t*-tests

Frog	Peak $\mathbf{T}_{translational}$ *vs* peak $\mathbf{T}_{rotational}$	$I_{translational}$ *vs* $I_{rotational}$	I_{drag} *vs* I_{amass}
1	0.0278*	0.0047*	0.0008*
2	0.0029*	0.0008*	0.1505
3	0.0497*	0.0051*	0.2127
4	0.0162*	0.0006*	0.9606

T is thrust, *I* is impulse, amass is added mass.
*Significant ($P<0.05$) from paired *t*-test.

and rotational velocity, simulated swimming velocity peaked at 35% of maximal velocity (Fig. 5B).

In all simulations, swimming velocity increased to a peak (positive acceleration) then decreased (deceleration) during the power stroke. This relative slowing [100%×(peak COM velocity – final COM velocity)/peak COM velocity] increased from 32% to 45% to 62% as the translational velocity was increased from 0 to 50% to 100% maximum (Fig. 5).

Simulated variation of translational and rotational velocity also strongly affected the thrust profile and the underlying components of thrust (added mass and drag). In each power stroke model, thrust increased in the first half of the stroke, peaked prior to peak COM velocity and fell to a negative peak near the end of the stroke (Fig. 5). Comparing the pure translation to the pure rotation case (Fig. 5A *vs* Fig. 5C), added mass thrust contributed most significantly to overall thrust during pure translation, with a peak added mass to peak drag thrust ratio of 1.7, as opposed to a ratio of 0.5 in the pure rotational case. Since peak added mass thrust preceded peak drag-based thrust in all simulations, this change in the relative contributions of these hydrodynamic components caused a corresponding shift in the timing of peak thrust from 0.33 to 0.36 s in the pure translation *vs* the pure rotation model, respectively. Additionally, the ratio of peak positive thrust to peak negative thrust decreased from 2.9 to 2.0 to 1.5 as the ratio of translational to rotational velocity was increased from 0:1 to 1:1 to 1:0, corresponding to the increased negative added mass thrust incurred by translational motion (Fig. 5).

Hypothetical anuran swimming performance space

The dependence of two performance parameters, peak stroke velocity (the peak swimming velocity reached in the stroke), and glide velocity (the final stroke velocity at the end of the power stroke), was tested against the relative magnitude of translational *vs* rotational foot velocity. As reported above, stroke velocity peaked before the end of limb extension. Consequently, in all simulations the velocity entering the glide phase was less than peak stroke velocity. Both of these parameters depended strongly on the magnitudes of translational and rotational foot velocity, with maximal performance predicted at the highest translational and rotational velocity (Fig. 7). Peak stroke velocity increased linearly (as indicated by the parallel straight diagonal contour lines) with peak translational velocity, but more strongly with rotational velocity. Partial least squares regression indicated that 60% of the variation in peak stroke velocity (among the 1089 simulated trials) was modulated by changes in rotational velocity alone. The swimming stroke powered by maximum foot translational velocity (zero rotation) reached 31% of the maximal velocity achieved with full rotation and translation, whereas maximal pure rotation produced a peak stroke velocity of 45% maximum (Fig. 7A). In contrast, pure translational velocity produced a glide velocity of only 15% maximum compared with 44% maximum with pure rotational velocity (Fig. 7B). Moreover, 76% of the variation in glide velocity (compared with 60% of variation in peak stroke velocity) was explained by modulation of rotational velocity.

Joint work, COM work and hydrodynamic efficiency

The simulated work done to move the animal's body was highest for the stroke powered by maximal foot translation and rotation (Fig. 8A). Similarly, the predicted combined net joint work required from muscles acting at the hip, knee and ankle was also highest when the foot was driven to maximal rotation and translation (Fig. 8B). For both joint and COM work, the increasing magnitude of contour lines was skewed toward maximal translation and rotation. Variation in COM work (among the 1089 simulations) was slightly more sensitive to changes in rotational (explaining 61% of variation in joint work) than translational foot velocity. However, translational and rotational foot velocity had nearly the same effect on simulated joint work. Simulated efficiency (COM work/net joint work) was almost entirely a function of rotational velocity, with maximal efficiency predicted for strokes with maximum rotational velocity and ~50% maximum translational velocity (Fig. 8C). Moreover, percentage deceleration was mainly dependent on

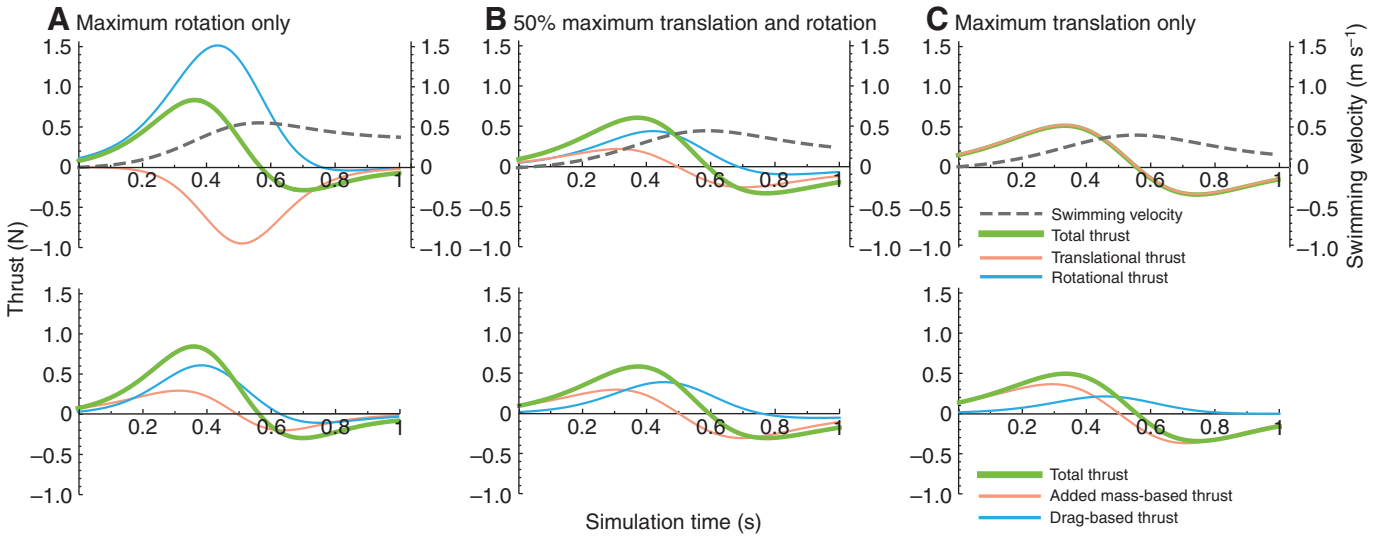

Fig. 5. Simulated anuran swimming. Power strokes are shown for three different conditions: (A) maximum foot rotation with no translation, (B) 50% maximum translation and rotation, (C) maximum translation with no rotation. For all conditions, top panels show swimming velocity traces (dashed black line), total thrust (green line), and translational (red line) and rotational components of thrust (blue line). Bottom panels show total thrust (green line), and added mass-based (red line) and drag-based (blue line) thrust. Translational and rotational velocities are in phase for all conditions shown. Note that total thrust traces are identical for top and bottom panels.

rotational velocity, with the highest values predicted for simulations lacking rotational foot motion (Fig. 8D).

DISCUSSION

The hydrodynamics of *Xenopus laevis* swimming

This study aimed to dissect the relative importance of translational *vs* rotational foot motion in the propulsion of an obligate swimmer, *Xenopus laevis*. Based on observations made in ranid frogs (Peters et al., 1996; Johansson and Lauder, 2004; Nauwelaerts et al., 2005), hydrodynamic thrust was hypothesized to be produced mainly from foot translational velocity and acceleration early in the extension phase. Therefore, stroke-to-stroke increases in translational velocity were expected to cause increases in peak swimming speed. Data from this study do not support either hypothesis. In all of the stroke cycles observed, the thrust impulse produced by rotational motion was significantly higher than the translational impulse ($P<0.05$ for each frog; Table 3) and translational thrust impulse did not correlate with total thrust impulse ($r^2=0.01$, $P>0.05$, $N=23$ strokes pooled from four frogs). I propose that these disparities between the present findings and previous work may be attributed to differences in joint kinematics patterns as well as leg and foot morphology among anuran species.

A generalized model for anuran swimming performance

A generalized model for anuran swimming can be used to explore interactions between hydrodynamics and aspects of performance (e.g. swimming efficiency and speed). Recent studies have reported low hydrodynamic efficiency for rowing swimmers at high Reynolds number (Fish, 1996; Walker and Westneat, 2000). Consistent with these previous findings, simulations of anuran swimming from the current study predict that the total net work summed over all hind limb joints is high compared with the work required to move the

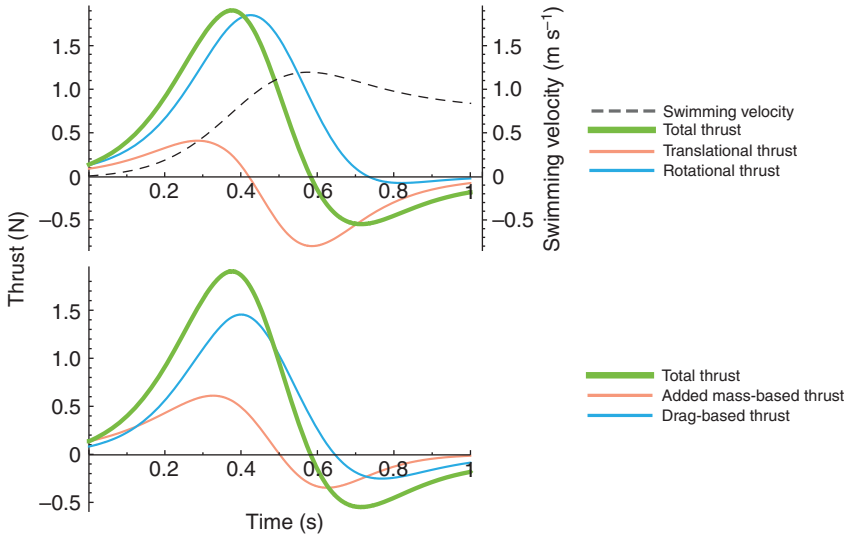

Fig. 6. Simulated anuran swimming during maximal foot translation and rotation. The top panel shows swimming velocity traces (dashed black line), total thrust (green line), and translational (red line) and rotational components of thrust (blue line). The bottom panel shows total thrust (green line), and added mass-based (red line) and drag-based (blue line) thrust. Translational and rotational velocities are in phase for all conditions shown. Note that total thrust traces are identical for top and bottom panels.

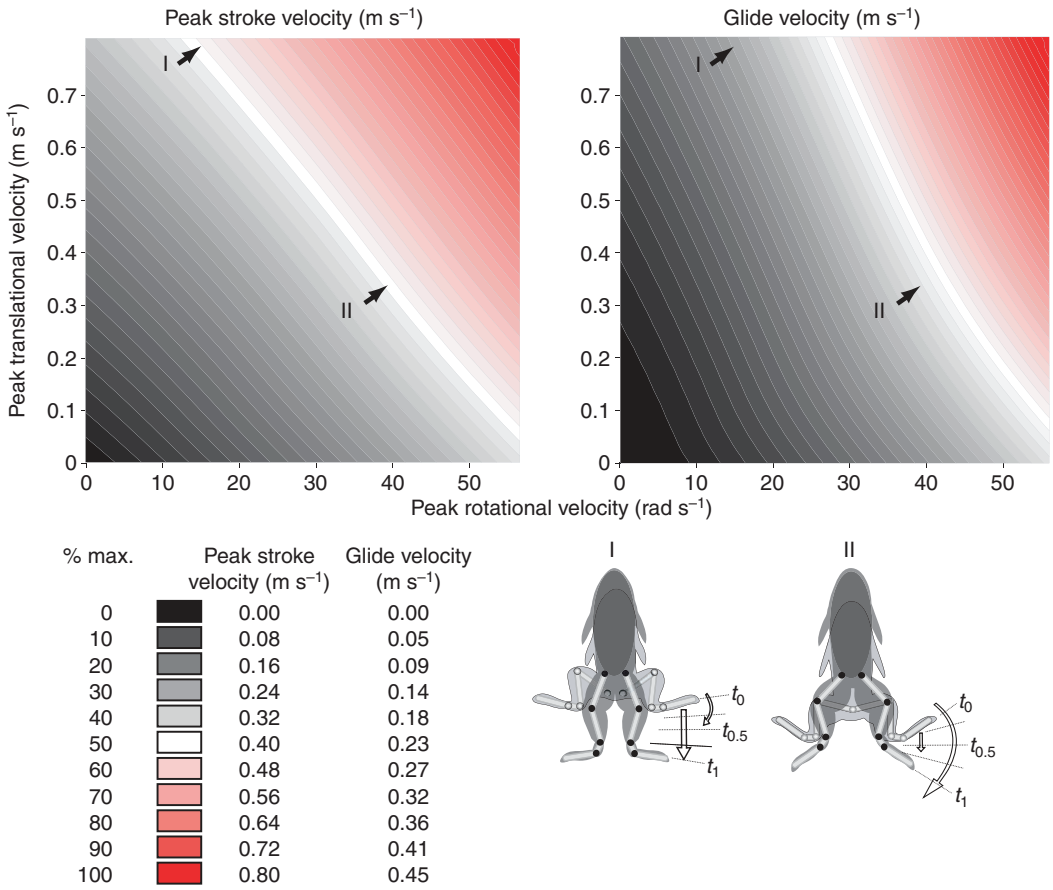

Fig. 7. Swimming performance space. Hypothetical maps of anuran swimming performance were generated from forward dynamic simulations run across a range of kinematic input conditions. Since only two input parameters were varied (amplitudes of trigonometric functions describing translational and rotational foot displacement), a 3D hypothetical space could be systematically explored by mapping a single output (such as peak simulated swimming velocity) against each of the two independently varied inputs: peak rotational (*x*-axis) and peak translational (*y*-axis) foot velocity. The initial foot angle for each simulation in the performance space was derived such that the foot is 90 deg. to flow at mid stroke ($t_{0.5}$) to decouple the effects of foot translation *vs* rotation. The color scale (from 0 to 100%) shows two performance parameters: (A) peak stroke swimming velocity and (B) glide velocity (the velocity at the end of the power stroke). Contour lines inclined more horizontally indicate a higher dependence on translational velocity, whereas more vertical lines indicate a higher dependence on rotational velocity. Arrows in A and B show different examples in the parameter space: arrow I shows large foot translation and small rotation, whereas arrow II shows large rotation and small translation. The corresponding diagrams show the path of foot motion throughout each simulated power stroke. These examples illustrate how two contrasting stroke patterns can have identical peak velocities (50% maximum) yet different glide velocities (~20% maximum *vs* 40% for examples I and II, respectively).

COM in a single stroke (Fig. 8A,B). This reflects the fact that additional work is required to overcome hydrodynamic resistance, as well as any work done by muscles to move body segments. As a result, efficiency is predicted to be low for anuran swimming over the range of kinematic conditions explored here (Fig. 8C).

The model was also used to address how swimming speed may be modulated by variation of kinematic patterns of the feet. Frog hind limbs have a wide range of joint configurations (Kargo and Rome, 2002) enabling a large repertoire of potential foot motion patterns. Using a forward dynamic model, one can map the relationship between foot kinematics and swimming speed by prescribing input joint kinematics and simulating the frog's swimming velocity output. This allows the examination of swimming hydrodynamics in the context of kinematic patterns that are anatomically possible, but not realized in actual *X. laevis* behavior. For example, simulations were bounded by two extreme hypothetical cases: (1) maximal foot translational velocity with no foot rotation (with minimal ankle action) and (2) maximal foot rotational velocity (with no hip or knee action). Surprisingly, swimming speed in the pure translation model was lower than in the opposite case of pure foot rotation (0.38 *vs* 0.54 m s^{-1}; Fig. 5A,C). There are two explanations for this result. Firstly, because the foot rotates very rapidly in *X. laevis* the maximal tangential rotational velocity (foot length × foot angular velocity) was much higher than the translational foot velocity. The highest values observed in *X. laevis* swimming (thus the values used as maximum input values for the simulations) were 2.3 and 0.8 m s^{-1}, for tangential rotational and translational velocities, respectively (based on frog 1). Accordingly, peak thrust was higher in the pure rotational *vs* translational simulation (0.83 *vs* 0.50 N, respectively). Secondly, added mass-based and drag-based thrust are out of phase in the translational case, whereas they are nearly coincident in the rotational case, enhancing their cumulative contribution to total thrust (Fig. 5A,C).

In addition to peak stroke velocity, predicted glide distance was also considered an important performance parameter. Since there is no propulsion during the glide, distance is limited by glide velocity (defined as the swimming velocity at the end of the power stroke).

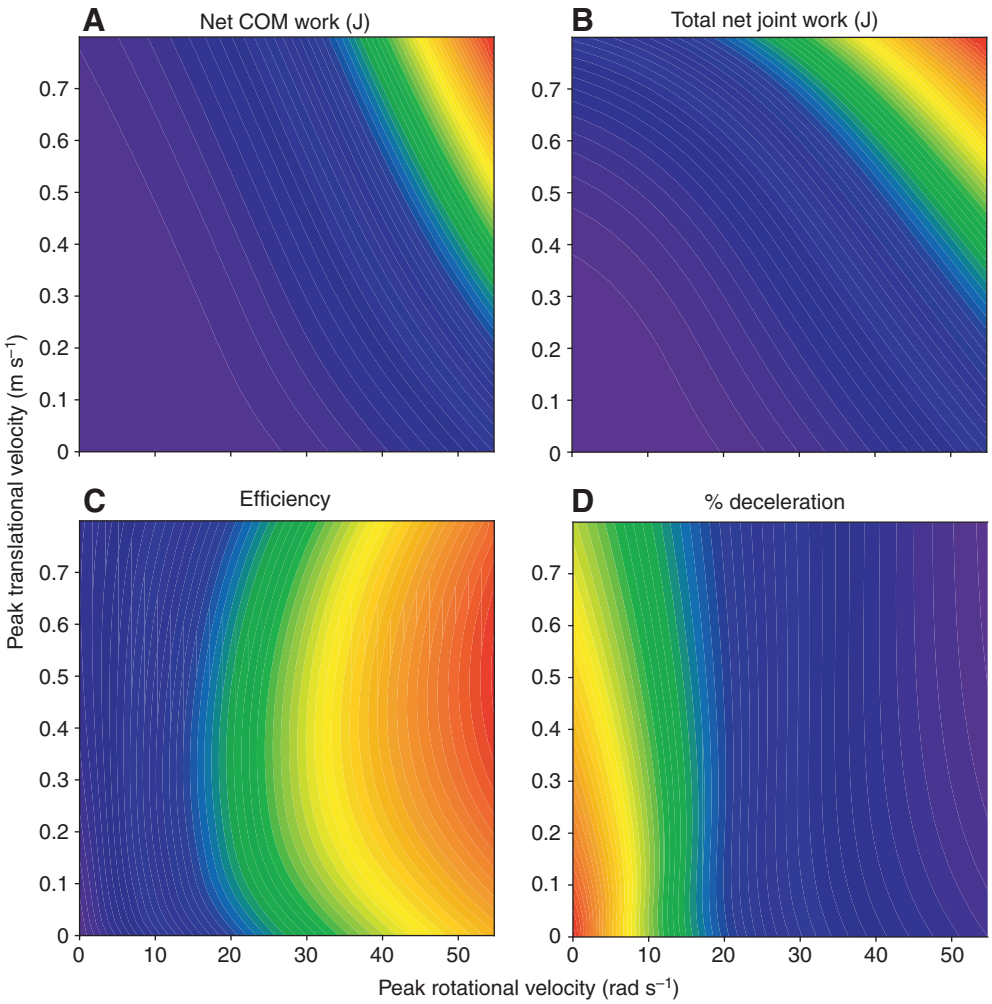

% max.	COM work (J)	Net joint work (J)	Efficiency	% deceleration
0	0.00000	1.10e–2	0.000	44.0
10	0.00037	2.20e–2	0.003	49.5
20	0.00074	3.30e–2	0.006	55.0
30	0.00111	4.40e–2	0.009	60.5
40	0.00148	5.50e–2	0.012	66.0
50	0.00185	6.60e–2	0.015	71.5
60	0.00222	7.70e–2	0.018	77.0
70	0.00259	8.80e–2	0.021	82.5
80	0.00296	9.90e–2	0.024	88.0
90	0.00333	1.10e–1	0.027	93.5
100	0.00370	1.21e–1	0.030	99.0

Fig. 8. Predicted mechanical work and efficiency of anuran swimming. As in Fig. 7, contour plots show peak rotational (*x*-axis) and peak translational velocity (*y*-axis) resulting from incrementally varying the input translational and rotational displacements in the numerical model. The color scale (from 0 to 100%) shows (A) net COM work (hydrodynamic and inertial forces acting on the body × total distance traveled) over each power stroke, (B) total net joint work (the sum of work produced at the hip, knee and ankle) over each power stroke, (C) net efficiency (net COM work/total net joint work) and (D) percentage deceleration [100%×(peak COM velocity – final COM velocity)/peak COM velocity].

In all power stroke simulations, the thrust impulse was positive for the first half of the stroke and negative for the second half. Because positive thrust always exceeded negative thrust, the net impulse was always positive, resulting in forward swimming velocity throughout each stroke. In the pure foot translational simulation (Fig. 5C), peak negative thrust reached 70% of peak positive thrust. During this stroke, aft-directed translational foot velocity exceeded forward COM velocity, so that the net translational foot velocity (foot translational velocity – COM velocity) was positive throughout limb extension and no negative drag was produced. Therefore, importantly, foot orientation 90 deg. to the flow did not cause drag retarding the forward movement of the body during the power stroke. In this case, negative thrust was produced entirely from added mass effects resulting from foot deceleration (i.e. positive, but decreasing translational velocity). In contrast, the simulation with sub-maximal foot translational and rotational velocities (Fig. 5B) reached a forward COM velocity that exceeded the rearward foot translational velocity, resulting in negative drag-based thrust (due to negative net translational velocity) in addition to negative added mass-based thrust (due to foot deceleration).

Searching the hypothetical performance space between the extremes of foot motion provides additional insights into the control of swimming performance. Fish increase swimming speed by increasing their stroke frequency (Brill and Dizon, 1979; Rome et al., 1984; Altringham and Ellerby, 1999; Swank and Rome, 2000). Although variation in stroke frequency also occurs in frogs, the

relationship between power stroke period and performance is unclear (Nauwelaerts et al., 2001). To avoid potentially confounding effects of stroke duration, power stroke simulations were run at a constant duration. As expected, simulations with proportional increases in translational and rotational amplitude (i.e. moving upwards and rightwards through the parameter space; Fig. 7A) predict a linear increase in peak stroke swimming velocity, as indicated by the diagonal contour lines. However, predicted glide performance did not follow the same trend (Fig. 7B). Glide velocity was disproportionately lower than peak stroke velocity in translation-dominated strokes, especially in the upper left quadrant of the performance space. In these strokes, rotational motion is too minimal to counteract the retarding thrust (from relatively large negative force due to foot translational deceleration; see above). Therefore, the highest COM deceleration during the power stroke is predicted to occur in the absence of foot rotation (being largely independent of translational velocity; Fig. 8D).

By predicting the hydrodynamic roles of translational *vs* rotational foot motion, this forward dynamic simulation provides a framework for understanding the kinematic determinants of thrust observed in frog swimming.

Dissecting the propulsive mechanism of a generalized *Xenopus laevis* swimming stroke

Despite observed variation in the temporal patterns of all components of thrust across 23 strokes (N=4 frogs), most propulsive strokes show two main phases. In the initial phase (Fig. 3, stages I, II and III), acceleration of the COM is driven mainly by both net translational velocity and foot acceleration (both translational and rotational). Propulsion in this phase, therefore, is dominated by translational drag and total added mass-based thrust. In the final phase (Fig. 3, stages IV and V), propulsion is enhanced and sustained by rotational velocity (generating rotational drag-based thrust), which usually peaks later than translational velocity. In all strokes observed, net translational velocity peaked in the first phase, but rapidly decreased to negative values in the second phase of the stroke as the forward velocity of the COM exceeded the backward translational velocity of the foot. This has two effects: (1) negative net translational velocity produces negative drag-based thrust and (2) translational deceleration (caused by the slowing translational foot motion toward the end of the power stroke) results in negative added mass-based thrust. Therefore, the kinematic components of thrust have unique roles in propulsion: early translational and rotational motion accelerate the frog at the onset of swimming. As foot rotational velocity increases later in the stroke, drag-based rotational thrust counteracts and overcomes the negative components of thrust, causing propulsion to continue until the end of the power stroke.

Linking kinematic plasticity to hydrodynamics: a proposed mechanism for modulating swimming performance from stroke to stroke

Xenopus laevis hind limb kinematics are highly variable, even within the behavioral subset of forward, straight and synchronous swimming. In contrast with the reported 'stereotypic' nature of *Hymenochirus boettgeri* (Gal and Blake, 1988b), *X. laevis* modulate time-varying flexion–extension patterns of the hind limb joints between sequential kicks of a single swimming burst (C.T.R., unpublished observations). Because foot motion is the sum of motion produced at the hip, knee, ankle and tarsometatarsal joints, the relative phases and magnitudes of translational and rotational velocity vary greatly from stroke to stroke in *X. laevis* (Table 1). Despite this variability, trends emerge. Most notably, peak stroke translational and rotational velocity are positively correlated across all swimming speeds and individuals (r^2=0.71, P<0.0001, pooled data from 23 swimming strokes, N=4 frogs). Further, peak COM velocity correlates with peak translational velocity (r^2=0.81, P<0.0001) and peak rotational velocity (r^2=0.66, P<0.0001), as well as with net thrust impulse (r^2=0.58, P<0.0001). Surprisingly, although peak translational and rotational velocity are correlated, the observed increase in thrust impulse among strokes is explained only by increases in rotational thrust impulse (r^2=0.71, P<0.0001). Total thrust impulse is independent of translational thrust impulse among the strokes analyzed (r^2=0.01, P=0.63). This suggests that correlative observations of kinematics and performance can be misleading in the absence of a more detailed hydrodynamic analysis. Despite the co-variation of translational, rotational and COM velocity, the underlying drive that provides increased net thrust from one stroke to the next is the increase of rotational impulse alone. For any given *X. laevis* stroke, the time-varying pattern of thrust depends on both translational and rotational foot motion. However, the shift between slow and fast swimming appears to require only an increase in net rotational thrust.

Hydrodynamic model verification and comments on Gal and Blake's model

Before applying the hydrodynamic model to resolve thrust components in *X. laevis* swimming, the model was verified using a modified implementation of Gal and Blake's approach (Gal and Blake, 1988b) to determine whether the model adequately estimated the temporal pattern of propulsive hydrodynamic force during *Xenopus laevis* swimming. Differing from that of Gal and Blake (Gal and Blake, 1988b), the modified blade element model was coupled to a forward dynamic model to simulate swimming velocity profiles for comparison to actual velocity profiles from analyzed video sequences (see Materials and methods). Although this approach generally underestimated the hydrodynamic forces required to propel the animal, the average error between observed and simulated swimming velocity was low (Fig. 2D,E). Although improvements to this model may be made for future studies (see below), the current approach is sufficient to investigate the hydrodynamic mechanisms for *X. laevis* swimming examined here.

Gal and Blake (Gal and Blake, 1988a; Gal and Blake, 1988b) used an elegant approach to verify their quasi-steady blade element model. From analyzed video sequences they calculated the force balance on the frog's COM required to generate an observed swimming acceleration pattern. They found a considerable disparity between thrust estimated by their blade element model and thrust predicted from the force balance on the frog body. Thrust estimated from the blade element model peaked at the beginning of limb extension and fell to a minimum (negative thrust) towards the end of the power stroke. Conversely, COM thrust calculated from the force balance peaked at mid-stroke and remained positive throughout the limb extension period. Although Gal and Blake acknowledged potential error from their added mass calculations, they proposed that a jet (produced as the feet move toward the midline) may account for thrust not predicted from blade element theory (Gal and Blake, 1988a; Gal and Blake, 1988b). I propose two additional explanations for their findings. Firstly, Gal and Blake did not account for the rotational component of added mass-based thrust, which contributes substantially to thrust in *X. laevis* (71±26% of total added mass impulse) and, therefore, may be important in *Hymenochirus boettgeri*. Secondly, Gal and Blake's method for measuring COM velocity may not be accurate. They used the

animal's vent to mark the COM. However, if the mass of *H. boettgeri* hind limbs is a significant portion of whole body mass, motion of the legs would affect the COM position on the body. Consequently, as the legs extend backwards the COM would also shift back, causing COM velocity to be lower compared with the velocity of a fixed point on the body. In *X. laevis*, hind limb motion resulted in a 16% change in COM position relative to snout–vent body length. Because of this, small modifications to Gal and Blake's model were used to correct for these potential concerns. Nevertheless, despite these limitations, Gal and Blake's model is a highly useful tool for resolving the complex mechanism by which anurans propel themselves through water.

Further modifications to Gal and Blake's model

Small discrepancies between simulated and observed time-varying swimming velocity may be resolved by future modifications of Gal and Blake's model (Gal and Blake, 1988b). For example, foot shape was approximated as a flat plate, yet *X. laevis* feet are thin extensible membranes supported by flexible digits. Consequently, foot shape may be dynamically changed through the power stroke, possibly allowing the foot to form a concave surface in flow, thus increasing the foot's drag coefficient considerably. For example, fish pectoral fins show impressive flexibility, affecting the time-varying hydrodynamic performance of the hydrofoil (Lauder et al., 2006). Additionally, controlled changes in the adduction–abduction angle between digits may affect the foot's projected area into the flow, possibly increasing area near mid-stroke (maximizing drag-based thrust) then decreasing area at the end of the stroke (reducing the negative added mass-based thrust). Measurement of detailed 3D foot kinematics that better describe time-dependent hydrodynamic coefficients would improve the accuracy of the model. Furthermore, inputs to the model (e.g. initial joint positions, joint excursions and relative phases of joint motion) could also be expanded to better describe the complex kinematic variation observed both within and among anuran species.

Diversity of anuran propulsive mechanisms

Recent studies have used particular species as models to understand the generalized principles of anuran swimming. However, findings in *Rana pipiens* (Peters et al., 1996; Johansson and Lauder, 2004) and *Rana esculenta* (Nauwelaerts and Aerts, 2003; Nawelaerts et al., 2005; Stamhuis and Nauwelaerts, 2005) differ from observations made on pipid frogs, such as *Hymenochirus boettgeri* (Gal and Blake, 1988a; Gal and Blake, 1988b) and *Xenopus laevis* (this study). For example, flow analyses of frog swimming, using digital particle image velocimetry (Johansson and Lauder, 2004; Nauwelaerts et al., 2005), show no evidence for a central propulsive jet formed by hydrodynamic interactions of the two legs, as proposed in Gal and Blake (Gal and Blake, 1988b). Yet, the kinematics of *R. pipiens* and *R. esculenta* differ strikingly from those of *H. boettgeri*. Therefore, these species are unlikely to show similar propulsive mechanisms. Likewise, the predominance of rotational foot motion observed in *X. laevis* need not negate earlier findings (Peters et al., 1996; Johansson and Lauder, 2004; Nauwelaerts et al., 2005) that thrust is powered mainly by translational foot motion (*vs* rotational motion) in other species. Each of these species has a different limb morphology and employs unique kinematics patterns during swimming. These differences motivate continued exploration of the diversity of hydrodynamic mechanisms evolved in anuran swimming related to their morphological and ecological diversification.

APPENDIX A

Calculating added mass coefficients

The force required to overcome the foot's added mass was calculated by multiplying the translational and rotational added mass coefficients with their respective components of translational and rotational foot acceleration (MIT web-based open courseware: http://ocw.mit.edu/OcwWeb/Mechanical-Engineering/2-20Spring-2005/CourseHome/index.htm). The added mass tensor was derived according to slender body theory (Newman, 1977) to resolve added mass coefficients for translational, rotational and coupled translation–rotation force components. Each added mass coefficient, m_{ij}, represents a component of added mass in the ith direction of translation (i=1 or 2 for cranio-caudal or medio-lateral translation, respectively) or rotation about the z-axis (i=6) causing a force in the jth direction. For example, m_{61} represents the added mass coefficient describing rotation about the z-axis causing an aft-directed force. Because the limb was assumed to move only in the frog's frontal plane (1–2 plane), only two components of translation i=1 (cranio-caudal axis) and i=2 (medio-lateral axis) and a single rotational component i=6 (ankle flexion–extension axis) were required to give the added mass tensor:

$$m_{11} = \rho\pi \sin^2\theta_f \int_0^c \left(\frac{b-a}{c}r + a\right)^2 dr\,, \quad \text{(A1)}$$

$$m_{12} = \rho\pi \sin 2\theta_f \int_0^c \left(\frac{b-a}{c}r + a\right)^2 dr\,, \quad \text{(A2)}$$

$$m_{22} = \rho\pi \cos^2\theta_f \int_0^c \left(\frac{b-a}{c}r + a\right)^2 dr\,, \quad \text{(A3)}$$

$$m_{61} = \rho\frac{\pi}{2}\sin\theta_f \int_0^c r\left(\frac{b-a}{c}r + a\right)^2 dr\,, \quad \text{(A4)}$$

$$m_{62} = -\rho\frac{\pi}{2}\cos\theta_f \int_0^c r\left(\frac{b-a}{c}r + a\right)^2 dr\,, \quad \text{(A5)}$$

and

$$m_{66} = \rho\frac{\pi}{3}\int_0^c r^2\left(\frac{b-a}{c}r + a\right)^2 dr\,, \quad \text{(A6)}$$

where θ_f is the angle of the foot (with respect to the body midline), ρ is water density, r is the distance from the ankle joint and a, b and c are dimensions of the foot (Fig. 1).

APPENDIX B

Inverse dynamics calculations

The moment of inertia for each segment was calculated as follows (Van Wassenbergh et al., 2008):

$$I = m\left(\frac{l^2}{16} + \frac{r_s^2}{12} + r^2\right)\,, \quad \text{(B1)}$$

where m is the segment's mass, l is the segment's length, r_s is the cylindrical segment's radius and r is the distance from the joint's center of rotation to the segment COM. Hydrodynamic drag and added mass resisting the motion of the leg segments was also considered. The leg segments were modeled as cylinders matching the average dimensions of *Xenopus laevis* hind limb segments. Drag was estimated by the method outlined by Gal and Blake (Gal and

Blake, 1988b) and added mass of each segment was estimated as the volume of the cylindrical segment (Newman, 1977):

$$\text{amass}_{\text{segment}} = \rho\pi r_s^2 l \ , \qquad \text{(B2)}$$

where ρ is the water density, r_s is the cylindrical segment's radius and l is the segment's length.

The hydrodynamic center of pressure (COP) on the foot was estimated as the weighted average of incremental forces (due to drag and added mass) occurring along the length of the foot:

$$\text{COP}_{\text{hydrodynamic}} = \frac{\int_0^c r(\mathbf{F}_{\text{drag}} + \mathbf{F}_{\text{amass}})\text{d}r}{\int_0^c (\mathbf{F}_{\text{drag}} + \mathbf{F}_{\text{amass}})\text{d}r} \ , \qquad \text{(B3)}$$

where r is the distance from the ankle joint, c is the length of the foot (see Fig. 1) and $\mathbf{F}_{\text{drag}}$ and $\mathbf{F}_{\text{amass}}$ are forces to overcome drag and added mass occurring at each blade element.

I thank Pedro Ramirez for animal care and Andrew Biewener for critical feedback, guidance and mentorship throughout this work as well as important comments during the preparation of this manuscript. I greatly thank Jack Dennerlein for invaluable assistance with the forward dynamic modeling as well as useful discussions regarding joint biomechanics. I also thank Craig McGowan for providing conceptual insights at the onset of this work, as well as helpful comments on the manuscript. I thank Brian Joo for assistance with data collection. Two anonymous reviewers provided detailed and thoughtful comments that helped clarify and strengthen this manuscript. This work was supported by the National Science Foundation's Integrative Graduate Education and Research Traineeship (IGERT) program, the Chapman Fellowship and the Department of Organismic and Evolutionary Biology at Harvard.

REFERENCES

Altringham, J. and Ellerby, D. (1999). Fish swimming: patterns in muscle function. *J. Exp. Biol.* **202**, 3397-3403.
Andersen, A., Pesavento, U. and Wang, Z. J. (2005). Unsteady aerodynamics of fluttering and tumbling plates. *J. Fluid Mech.* **541**, 65-90.
Biewener, A. and Baudinette, R. (1995). *In vivo* muscle force and elastic energy storage during steady-speed hopping of tammar wallabies (*Macropus eugenii*). *J. Exp. Biol.* **198**, 1829-1841.
Biewener, A. and Full, R. J. (1992). Force platform and kinematic analysis. In *Biomechanics* (ed. A. Biewener), pp. 45-73. New York: Oxford University Press.
Blake, R. W. (1979). The mechanics of labriform locomotion i. Labriform locomotion in the angelfish (*Pterophyllum eimekei*): an analysis of the power stroke. *J. Exp. Biol.* **82**, 255-271.
Blake, R. W. (1985). Hydrodynamics of swimming in the water boatman, *Cenocorixa bifida*. *Canadian J. Zool.* **64**, 1606-1613.
Brill, R. W. and Dizon, A. E. (1979). Red and white muscle fibre activity in swimming skipjack tuna, *Katsuwonus pelamis* (L.). *J. Fish Biol.* **15**, 679-685.
Daley, M. A., Felix, G. and Biewener, A. A. (2007). Running stability is enhanced by a proximo-distal gradient in joint neuromechanical control. *J. Exp. Biol.* **210**, 383-394.
Daniel, T. L. (1984). Unsteady aspects of aquatic locomotion. *Am. Zool.* **24**, 121-134.
Dutto, D. J., Hoyt, D. F., Clayton, H. M., Cogger, E. A. and Wickler, S. J. (2006). Joint work and power for both the forelimb and hindlimb during trotting in the horse. *J. Exp. Biol.* **209**, 3990-3999.
Fish, F. (1996). Transitions from drag-based to lift-based propulsion in mammalian swimming. *Am. Zool.* **36**, 628-641.
Fish, F., Baudinette, R., Frappell, P. and Sarre, M. (1997). Energetics of swimming by the platypus *Ornithorhynchus anatinus*: metabolic effort associated with rowing. *J. Exp. Biol.* **200**, 2647-2652.
Gal, J. M. and Blake, R. W. (1988a). Biomechanics of frog swimming: I. Estimation of the propulsive force generated by *Hymenochirus Boettgeri*. *J. Exp. Biol.* **138**, 399-411.
Gal, J. M. and Blake, R. W. (1988b). Biomechanics of frog swimming: II. Mechanics of the limb-beat cycle in *Hymenochirus Boettgeri*. *J. Exp. Biol.* **138**, 413-429.
Johansson, L. and Lindhe Norberg, U. M. (2001). Lift-based paddling in diving grebe. *J. Exp. Biol.* **204**, 1687-1696.
Johansson, L. C. and Lauder, G. V. (2004). Hydrodynamics of surface swimming in leopard frogs (*Rana pipiens*). *J. Exp. Biol.* **207**, 3945-3958.
Johansson, L. C. and Norberg, R. A. (2003). Delta-wing function of webbed feet gives hydrodynamic lift for swimming propulsion in birds. *Nature* **424**, 65.
Kargo, W. K. and Rome, L. C. (2002). Functional morphology of proximal hindlimb muscles in the frog *Rana pipiens*. *J. Exp. Biol.* **205**, 1987-2004.
Lauder, G. V., Madden, P. G., Mittal, R., Dong, H. and Bozkurttas, M. (2006). Locomotion with flexible propulsors: I. Experimental analysis of pectoral fin swimming in sunfish. *Bioinspir. Biomim.* **1**, s25-s34.
McGowan, C. P., Baudinette, R. V. and Biewener, A. A. (2005). Joint work and power associated with acceleration and deceleration in tammar wallabies (*Macropus eugenii*). *J. Exp. Biol.* **208**, 41-53.
Nauwelaerts, S. and Aerts, P. (2003). Propulsive impulse as a covarying performance measure in the comparison of the kinematics of swimming and jumping in frogs. *J. Exp. Biol.* **206**, 4341-4351.
Nauwelaerts, S., Aerts, P. and D'Août, K. (2001). Speed modulation in swimming frogs. *J. Mot. Behavior* **33**, 265-272.
Nauwelaerts, S., Stamhuis, E. J. and Aerts, P. (2005). Propulsive force calculations in swimming frogs I. A momentum-impulse approach. *J. Exp. Biol.* **208**, 1435-1443.
Newman, J. N. (1977). *Marine Hydrodynamics*. Cambridge: The MIT Press.
Pace, C. M., Blob, R. W. and Westneat, M. W. (2001). Comparative kinematics of the forelimb during swimming in red-eared slider (*Trachemys scripta*) and spiny softshell (*Apalone spinifera*) turtles. *J. Exp. Biol.* **204**, 3261-3271.
Peters, S. E., Kamel, L. T. and Bashor, D. P. (1996). Hopping and swimming in the Leopard Frog, *Rana pipiens*: I. Step Cycles and Kinematics. *J. Morphol.* **230**, 1-16.
Richards, C. T. and Biewener, A. A. (2007). Modulation of in vivo muscle power output during swimming in the African clawed frog (*Xenopus laevis*). *J. Exp. Biol.* **210**, 3147-3159.
Roberts, T. J. and Belliveau, R. A. (2005). Sources of mechanical power for uphill running in humans. *J. Exp. Biol.* **208**, 1963-1970.
Roberts, T. J. and Scales, J. A. (2004). Adjusting muscle function to demand: joint work during acceleration in wild turkeys. *J. Exp. Biol.* **207**, 4165-4174.
Rome, L. C., Loughna, P. T. and Goldspink, G. (1984). Muscle fiber activity in carp as a function of swimming speed and muscle temperature. *Am. J. Physiol. Regul. Integr. Comp. Physiol.* **247**, R272-R279.
Stamhuis, E. J. and Nauwelaerts, S. (2005). Propulsive force calculations in swimming frogs II. Application of a vortex ring model to DPIV data. *J. Exp. Biol.* **208**, 1445-1451.
Swank, D. and Rome, L. (2000). The influence of temperature on power production during swimming. I. In vivo length change and stimulation pattern. *J. Exp. Biol.* **203**, 321-331.
Van Wassenbergh, S., Strother, J. A., Flammang, B. E., Ferry-Graham, L. A. and Aerts, P. (2008). Extremely fast prey capture in pipefish is powered by elastic recoil. *J. R. Soc. Interface* **5**, 285-296.
Vogel, S. (1994). *Life in Moving Fluids*. Princeton: Princeton University Press.
Walker, J. A., Westneat, M. W. (2000). Mechanical performance of aquatic rowing and flying. *Proc. R. Soc. Lond., B, Biol. Sci.* **267**, 1875-1881.
Walker, J. A. and Westneat, M. W. (2002). Performance limits of labriform propulsion and correlates with fin shape and motion. *J. Exp. Biol.* **205**, 177-187.
Walter, R. M. and Carrier, D. R. (2002). Scaling of rotational inertia in murine rodents and two species of lizard. *J. Exp. Biol.* **205**, 2135-2141.